Supporting Information

Directing group-assisted *para*-selective C−H alkynylation of unbiased arenes enabled by rhodium catalysis

Uttam Dutta,[a]# Gaurav Prakash,[a]# Kirti Devi,[a] Kongkona Borah,[a] Xinglong Zhang,*[b] Debabrata Maiti*[a]

[a] Dr. U. Dutta, G. Prakash, K. Devi, K. Borah, Prof. Dr. D. Maiti
Department of Chemistry, Indian Institute of Technology Bombay
Powai, Mumbai-400076 (India)
[b] Institute of High Performance Computing, Agency for Science, Technology and Research (A*STAR), 1 Fusionopolis Way,
    #16−16 Connexis, Singapore-138632
E-mail: zhang_xinglong@ihpc.a-star.edu.sg (XZ), dmaiti@iitb.ac.in (DM)
# These authors contributed equally.

6. Computational Methods

Density functional theory (DFT) calculations were performed with *Gaussian 16* rev. B.01.[12] Geometry optimizations were initially performed using the global-hybrid meta-NGA (nonseparable gradient approximation) MN15 functional[13] with the def2-SVP[14,15] Karlsruhe-family basis set and the optimized structures further refined with a mix of larger basis set consisting of triple-ζ valence def2-TZVPD (where 'D' indicates diffuse basis functions) for Br[16], Rh[17,18] and Ag[16,17] atoms and def2-SVP[14,15] for all other atoms (BS1). MN15 functional was chosen as it performs much better than many other functionals (e.g. ωB97X-D and TPSS) in predicting transition metal (TM) reaction barrier heights and giving better geometries for both TM complexes and organic molecules.[2] Minima and transition structures on the potential energy surface (PES) were confirmed using harmonic frequency analysis at the same level of theory, showing respectively zero and one imaginary frequency. Where appropriate for cases where visual inspection of TS imaginary frequency is not obvious (e.g., for the beta-bromide elimination TS), intrinsic reaction coordinate (IRC) analyses[18,19] were performed to confirm that the found TSs connect to the right reactants and products. Single point (SP) corrections were performed using MN15 functional and def2-QZVP[14] basis set for all atoms. The SMD implicit continuum solvation model[20] was used to account for the effect of dichloroethane solvent on the computed Gibbs energy profile. Gibbs energies were evaluated at the reaction temperature of 393.15 K (120°C), using a quasi-RRHO treatment of vibrational entropies.[21,22] Vibrational entropies of frequencies below 100 cm^{-1} were obtained according to a free rotor description, using a smooth damping function to interpolate between the two limiting descriptions. The free energies were further corrected using standard concentration of 1 mol/L, which were used in solvation calculations. Unless otherwise stated, the final SMD (dichloroethane)-MN15/def2-QZVP//MN15/BS1 Gibbs energies are used for discussion throughout. *All Gibbs energy values in the text and figures are quoted in kcal mol^{-1}*. Molecular orbitals are generated from solvent-corrected SMD(1,4-dioxane)-MN15/def2-QZVPP checkpoint files and visualized using an isosurface value of 0.05 throughout. All molecular structures and molecular orbitals were visualized using *PyMOL* software.[23]

Geometries of all optimized structures (in *.xyz* format with their associated energy in Hartrees) are included in a separate folder named *DFT_structures*. All these data have been deposited with this Supporting Information and uploaded to zenodo.org under https://zenodo.org/record/7585280.

6.1 Model Simplification and Conformational considerations

Structure **SM1**, where the isopropyl (^{i}Pr) groups on the Si-atom are replaced by methyl (Me) groups, was used as a simplified model for computational modelling. The use of ^{i}Pr groups on Si probably benefits from favorable Thorpe–Ingold effect making the formation of rhodacycle easier than Me groups, but this simplification should not affect the reaction mechanism – any favorable barriers calculated with this simplified model are expected to be favorable for the ^{i}Pr analogue as well. The adamantane-1-carboxylate is simplified to acetate to save computational cost. The adamantyl group provides sterics to the molecules and in computational modelling we avoid conformations with any possible clashes that would arise if adamantane-1-carboxylate was used instead of acetate.

The starting material for computational modelling, **SM1**, was first conformationally sampled. The possible rotamers for **SM1** were generated by systematically varying a combination of key dihedral angles shown in red (Scheme S9) and optimizing the structures. The lowest energy conformer was used for subsequent calculations. For the Rh complexes involved in the reaction, such as **INT1** shown, the conformational flexibility is rather limited due to the rigidity of the coordinating sites of substrate **SM1** to Rh metal center. The conformations of the coordinating substrate (shown in blue in Scheme S9) are kept the same throughout the computational modelling.
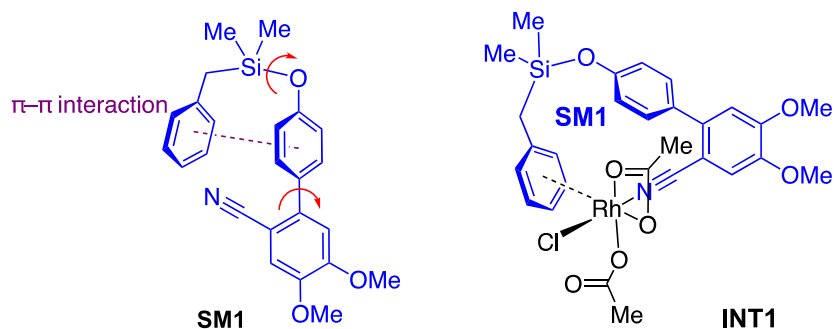

Scheme S9. Rotamers were generated by varying the dihedral angles in red in conformational sampling of the most stable conformer used for reaction modelling.

6.2 Rh(III) species in the reaction

Figure S4 compares the relative energies of the different species of rodacycles with varying coordinating ligands occupying different coordination sites. **INT1**, having Cl$^-$ anion as one of the ligands is the most stable species and this is used for computational mechanistic investigations.

The regioisomeric **INT1a**, where Cl⁻ anion is at a different coordination site (*cis* to the nitrile group), is 5.7 kcal mol⁻¹ higher in energy than where the Cl⁻ anion is *trans* to the nitrile group. The species with AcO⁻ anion instead of Cl⁻ anion, **INT1'**, is 21.4 kcal mol⁻¹ higher in energy. The corresponding high spin Rh-species of **INT1** is 86.9 kcal mol⁻¹ higher in energy and is thus not the ground state for this complex.
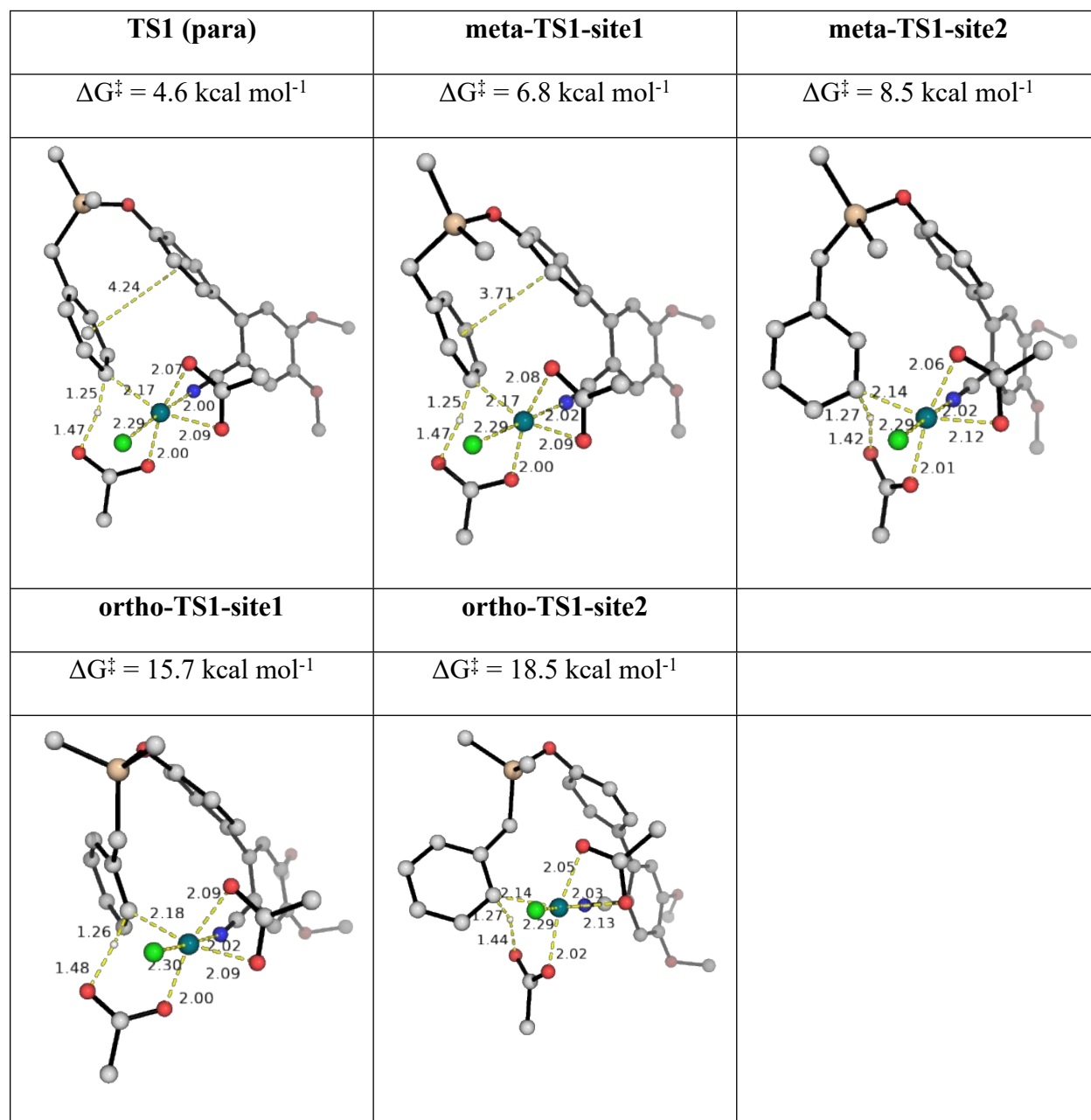
INT1	INT1'	INT1a
ΔΔG = 0.0 kcal mol⁻¹	ΔΔG = 21.4 kcal mol⁻¹	ΔΔG = 5.7 kcal mol⁻¹
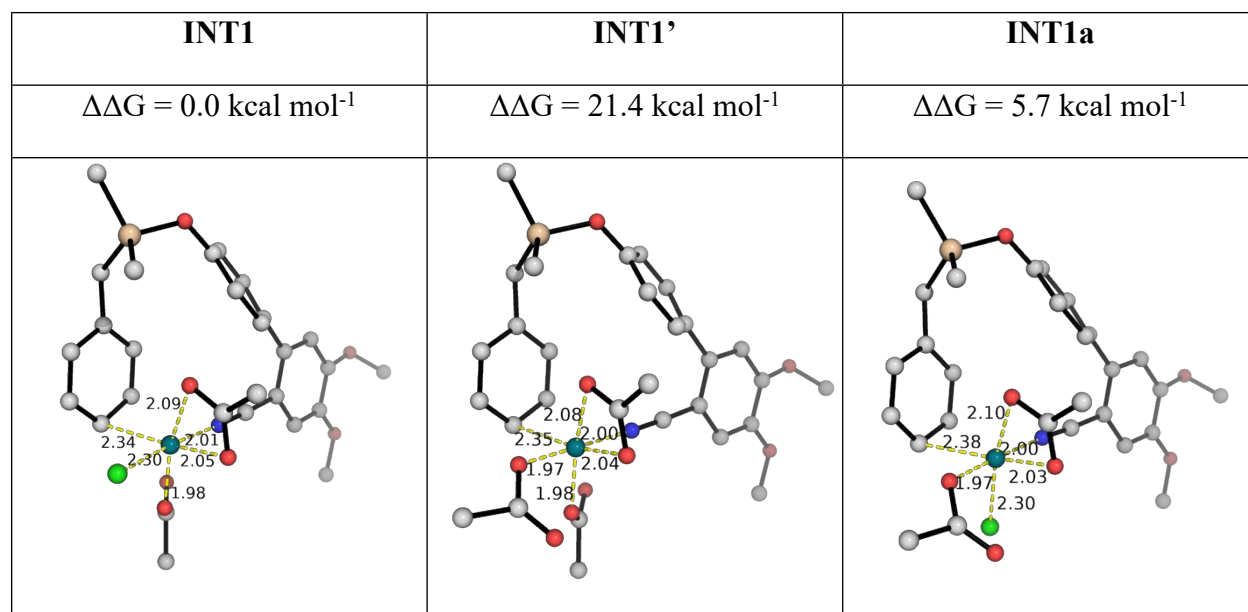
Figure S4. DFT optimized rodacyclic complexes. Relative Gibbs energies are given in kcal mol⁻¹.
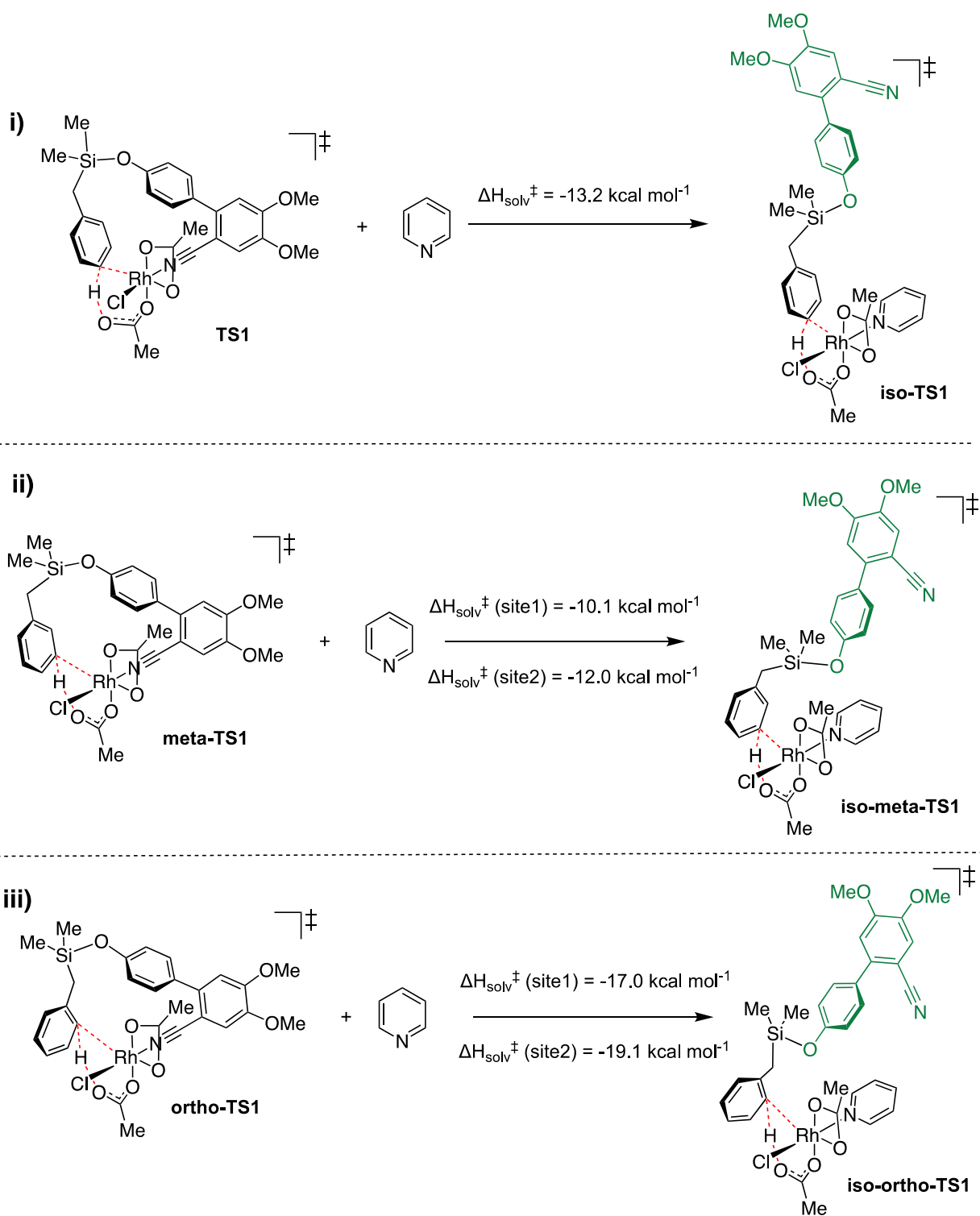
6.3 C–H activation step

Although the C–H activation step is not the overall rate-limiting step of the Rh-catalyzed alkynylation (Figure 1, main text), it is the regio-determining step, as the formation of the rhodacycle after C–H activation is highly exergonic and irreversible.

Figure S5 shows all the TSs for the C–H activation step. C–H activation at *para*-position has a barrier of 4.6 kcal mol⁻¹, while the lowest barrier for C–H activation at *meta*-position is 6.8 kcal mol⁻¹ (***meta*-TS1-site1**) and the lowest barrier for C–H activation at *ortho*-position is 15.7 kcal mol⁻¹ (***ortho*-TS1-site1**). This higher barrier of 2.2 kcal mol⁻¹ for *meta*- over *para*-selectivity indicates a 16:1 selectivity in favor of *para*-position over *meta*-position; the higher barrier of 11.1 kcal mol⁻¹ for *ortho*- over *para*-selectivity indicates a 1.5 milion:1 selectivity in favor of *para*-position over *ortho*-position.

Comparing the two *meta* TS (**meta-TS1-site1** and **meta-TS1-site2**) and the two *ortho* TSs (**ortho-TS1-site1** and **ortho-TS1-site2**), we can see that the more the arene is positioned away from the favorable π-π interaction with the phenyl ring on the directing group and the more the rhodacyle is twisted, the higher the activation barriers (**site2** TSs over and **site1** TSs).

TS1 (para)	meta-TS1-site1	meta-TS1-site2
$\Delta G^{\ddagger} = 4.6$ kcal mol^{-1}	$\Delta G^{\ddagger} = 6.8$ kcal mol^{-1}	$\Delta G^{\ddagger} = 8.5$ kcal mol^{-1}
ortho-TS1-site1	**ortho-TS1-site2**	
$\Delta G^{\ddagger} = 15.7$ kcal mol^{-1}	$\Delta G^{\ddagger} = 18.5$ kcal mol^{-1}	

Figure S5. DFT optimized TS structures for the C–H activation step at different arene sites.

Scheme S10. Computed ring strain involving a hypothetical pyridine ligand for the C–H activation step.

We further performed isodesmic studies[24,25] to estimate the ring strains in these C–H activation TSs: a hypothetical pyridine ligand was used to displace the Rh–N(nitrile) interaction in these TSs

to release the ring strain so that the directing group (DG) gets uncoordinated (Scheme S10, see refs[26,27] for examples of such calculations). The starting conformation for the DG (highlighted in green, Scheme S10) in all 3 cases was made the same in a linear geometry for subsequent TS searches. The enthalpies of the reactions were corrected with SMD solvation model:

$$\Delta H_{sol}^{\ddagger} = \Delta H_{gas}^{\ddagger} - \Delta E_{gas}^{\ddagger} + \Delta E_{sol}^{\ddagger}.$$

	Barrier	Barrier *relative* to para-activation	Ring strain	Ring strain *relative* to para-activation
TS1 (para)	4.6	0.0	13.2	0
meta-TS1-site1	6.8	2.2	10.1	-3.1
meta-TS1-site2	8.5	3.9	12.0	-1.2
ortho-TS1-site1	15.7	11.1	17.0	3.8
ortho-TS1-site2	18.5	13.9	19.1	5.9

Table S9. Comparison of relative barriers and computed ring strains from isodesmic studies for C–H activation TSs. All values are given in kcal mol^{-1}. Although C–H activation at *meta*-positions have higher barriers, they have smaller ring strains (highlighted in grey) compared to C–H activation at *para*-position.

From the enthalpic changes, we can see that there is 13.2 kcal mol^{-1} ring strain in **TS1** vs 10.1 kcal mol^{-1} in **meta-TS1-site1** and 17.0 kcal mol^{-1} in **ortho-TS1-site1**. These values are summarized in Table S9. From the table, we see that ring strain only contributes partially to the activation barrier heights in the current system: the *ortho*-C–H activations (**ortho-TS1-site1** and **ortho-TS1-site2**) have barriers 11.1 and 13.9 kcal mol^{-1} higher than *para*-C–H activation, however, ring strains are only 3.8 and 5. 9 kcal mol^{-1} respectively. In addition, the *meta*-C–H activations (**meta-TS1-site1** and **meta-TS1-site2**) have barriers 2.2 and 3.9 kcal mol^{-1} higher than *para*-C–H activation, but they both have lower ring strains than *para*-C–H activation. Therefore, electronic factors and non-covalent interactions could be important for the regioselectivities in the C–H activation step.

Figure S6 shows the HOMOs for the lowest energy TSs in the C–H activation step at various positions. These demonstrate that at the *para*-position, the orbital overlap is the best between the d-orbital on Rh-metal and the π-orbital on the arene, whereas the *meta*- and *ortho*- C–H activation

TSs have poor orbital overlap. Thus, the good orbital overlaps in *para*-C–H activation lowers the C–H activation barrier.
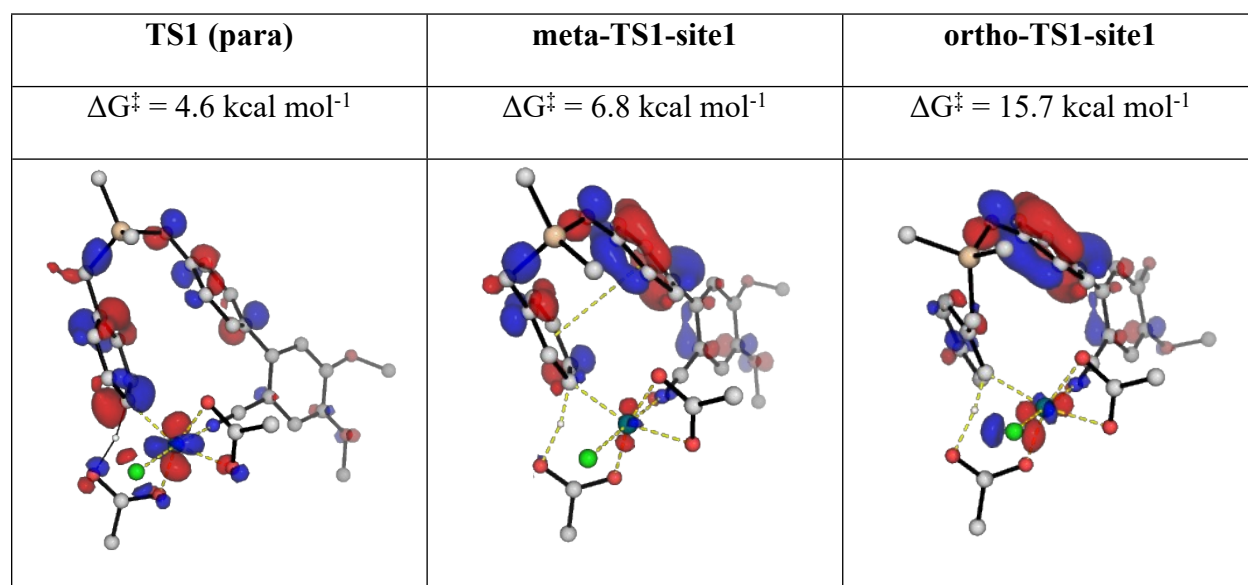
TS1 (para)	meta-TS1-site1	ortho-TS1-site1
$\Delta G^\ddagger = 4.6$ kcal mol^{-1}	$\Delta G^\ddagger = 6.8$ kcal mol^{-1}	$\Delta G^\ddagger = 15.7$ kcal mol^{-1}

Figure S6. HOMOs for the lowest energy C–H activation TSs at various positions at an isosurface value of 0.05.

6.4. Optimized structures and absolute energies, zero-point energies

Geometries of all optimized structures (in *.xyz* format with their associated energy in Hartrees) are included in a separate folder named *final_xyz_structures* with an associated readme.txt file. All these data have been deposited with this Supporting Information and uploaded to zenodo.org under https://zenodo.org/record/7585280 (DOI: 10.5281/zenodo.7585280).

Absolute values (in Hartrees) for SCF energy, zero-point vibrational energy (ZPE), enthalpy and quasi-harmonic Gibbs free energy (at 120°C/393.15 K) for optimized structures are given below. Single point corrections in SMD dichloroethane using MN15/def2-QZVP level of theory are also included.

Structure	E/au	ZPE/au	H/au	T.S/au	qh-G/au	SP MN15-2X/def2-QZVP
acetate	-228.059294	0.048236	-228.00312	0.042052	-228.044074	-228.58196816
cl_anion	-459.94618	0	-459.94307	0.019458	-459.962525	-460.35548536
acetic_acid	-228.644533	0.062197	-228.57411	0.041723	-228.61541	-229.06955302
para_prd	-1981.081338	0.546187	-1980.4703	0.171415	-1980.629273	-1984.01198130
SM1	-1496.88555	0.434538	-1496.4017	0.137658	-1496.530029	-1499.27458900

AgBr_monomer	-2721.225319	0.000564	-2721.2196	0.035623	-2721.255255	-2721.39785166
AgBr_dimer	-5442.524491	0.001782	-5442.5119	0.057735	-5442.568098	-5442.84035785
AgOAc_monomer	-374.748696	0.050645	-374.68765	0.052241	-374.738021	-375.18550671
AgOAc_dimer	-749.614004	0.104042	-749.48872	0.080731	-749.564698	-750.44446144
pyridine	-247.762761	0.089473	-247.66485	0.04235	-247.707207	-248.22280239
bromide_anion	-2574.568731	0	-2574.5656	0.020978	-2574.586596	-2574.79169029
INT1'	-2291.480019	0.593629	-2290.8113	0.19471	-2290.990623	-2295.11328959
INT1a	-2523.377463	0.543043	-2522.7649	0.182377	-2522.93338	-2526.87032898
INT1	-2523.387198	0.543315	-2522.7745	0.181615	-2522.942522	-2526.87365115
TS1	-2523.375553	0.538406	-2522.7684	0.181045	-2522.935902	-2526.86128572
INT2	-2523.422867	0.543207	-2522.8102	0.182821	-2522.978994	-2526.90216367
meta-TS1-site1	-2523.377822	0.538772	-2522.7706	0.178007	-2522.936478	-2526.85952134
meta-TS1-site2	-2523.370902	0.538089	-2522.7642	0.179235	-2522.930407	-2526.85587057
ortho-TS1-site1	-2523.363381	0.538104	-2522.7567	0.177348	-2522.923016	-2526.84425515
ortho-TS1-site2	-2523.357095	0.538074	-2522.7507	0.177225	-2522.916189	-2526.84047622
TIPS_ethynyl_bromide	-3294.590028	0.292704	-3294.266	0.096914	-3294.358717	-3295.72618549
INT3	-5589.359989	0.774064	-5588.4932	0.230722	-5588.706268	-5593.55152672
TS2	-5589.340178	0.772675	-5588.4754	0.230546	-5588.68775	-5593.53371449
INT4	-5589.391612	0.776455	-5588.5237	0.226948	-5588.733939	-5593.58151479
TS2-c2	-5589.336832	0.772709	-5588.4721	0.230284	-5588.684317	-5593.53129885
TS3	-5589.351953	0.774786	-5588.4857	0.226652	-5588.695722	-5593.551563
INT5	-5589.355253	0.774633	-5588.4877	0.233164	-5588.701594	-5593.556881
INT4prime	-5735.888644	0.776531	-5735.0173	0.23592	-5735.235146	-5740.141028
TS3prime	-5735.88473	0.775398	-5735.0148	0.236191	-5735.232237	-5740.13771
INT5prime	-5735.909927	0.775979	-5735.0381	0.243622	-5735.259463	-5740.170937
iso-meta-TS1	-2771.161608	0.629032	-2770.4539	0.208236	-2770.642855	-2775.10100132
iso-ortho-TS1	-2771.166312	0.629765	-2770.4587	0.200443	-2770.643758	-2775.09712330

7. References:

1. U. Dutta, S. Maiti, S. Pimparkar, S. Maiti, L. R. Gahan, E. H. Krenske, D.W. Lupton and D. Maiti, *Chem. Sci*. **2019**, *10*, 7426–7432;

2. S. Sasmal, G. Prakash, U. Dutta, R. Laskar, G. K. Lahiri, D. Maiti. *Chem. Sci.* **2022**, *13*, 5616-5621.

3. S. Bag, T. Patra, A. Modak, A. Deb, S. Maity, U. Dutta, A. Dey, R. Kancherla, A. Maji, A. Hazra, M. Bera, D. Maiti, *J. Am. Chem. Soc.* **2015**, *137*, 11888-11891.

4. C. Wang, H. Ge, *Chem. Eur. J.* **2011**, *17*, 14371 – 14374.

5. E. Richmond, J. Moran, *J. Org. Chem.* **2015**, *80*, 6922−6929.

6. U. Dutta, D. W. Lupton, D. Maiti, *Org. Lett.* **2016**, *18*, 860–863.

7. K. A. A. Kumara, V. Venkateswarlua, R. A. Vishwakarmaa, S. D. Sawant, *Synthesis* **2015**, *47*, 3161–3168

8. C. Li, P. Zhao, R. Li, B. Zhang, W. Zhao, *Angew. Chem. Int. Ed.* **2020**, *59*, 10913 –10917.

9. U. Dutta, S. Maity, R. Kancherla, D. Maiti, *Org. Lett.* **2014**, *16*, 6302–6305.

10. S. Madabhushi, R. Jillella, K. K. R. Mallu, K. R. Godala, V. S. Vangipuram, *Tetrahedron Letters* **2013,** *54*, 3993–3996.

11. S. Lin, M. Li, Z. Dong, F. Liang, J. Zhang, *Org. Biomol. Chem*., **2014**, *12*, 1341-1350.

Full reference Gaussian 16:

Gaussian 16, Revision B.01, Frisch, M. J.; Trucks, G. W.; Schlegel, H. B.; Scuseria, G. E.; Robb, M. A.; Cheeseman, J. R.; Scalmani, G.; Barone, V.; Mennucci, B.; Petersson, G. A.; Nakatsuji, H.; Caricato, M.; Li, X.; Hratchian, H. P.; Izmaylov, A. F.; Bloino, J.; Zheng, G.; Sonnenberg, J. L.; Hada, M.; Ehara, M.; Toyota, K.; Fukuda, R.; Hasegawa, J.; Ishida, M.; Nakajima, T.; Honda, Y.; Kitao, O.; Nakai, H.; Vreven, T.; Montgomery Jr., J. A.; Peralta, J. E.; Ogliaro, F.; Bearpark, M.; Heyd, J. J.; Brothers, E.; Kudin, K. N.; Staroverov, V. N.; Kobayashi, R.; Normand, J.; Raghavachari, K.; Rendell, A.; Burant, J. C.; Iyengar, S. S.; Tomasi, J.; Cossi, M.; Rega, N.; Millam, J. M.; Klene, M.; Knox, J. E.; Cross, J. B.; Bakken, V.; Adamo, C.; Jaramillo, J.; Gomperts, R.; Stratmann, R. E.; Yazyev, O.; Austin, A. J.; Cammi, R.; Pomelli, C.; Ochterski, J. W.; Martin, R. L.; Morokuma, K.; Zakrzewski, V. G.; Voth, G. A.; Salvador, P.; Dannenberg, J. J.; Dapprich, S.; Daniels, A. D.; Farkas, Ö.; Foresman, J. B.; Ortiz, J. V; Cioslowski, J.; Fox, D. J.

Gaussian, Inc., Wallingford CT, 2016.

(12)   M. J. Frisch, G. W. Trucks, H. B. Schlegel, G. E. Scuseria, M. A. Robb, J. R. Cheeseman, G. Scalmani, V. Barone, G. A. Petersson, H. Nakatsuji, et al. Gaussian 16, Revision B.01. 2016.

(13)   H. S. Yu, X. He, S. L. Li, D. G. Truhlar, MN15: *Chem. Sci.* **2016**, *7*, 5032–5051.

(14)   F. Weigend, R. Ahlrichs, *Phys. Chem. Chem. Phys.* **2005**, *7*, 3297–3305.

(15)   F. Weigend, Accurate Coulomb-Fitting Basis Sets for H to Rn.. **2006**, *8*, 1057–1065.

(16)   D. Rappoport, F. Furche, *J. Chem. Phys.* **2010**, *133*, 134105.

(17)   D. Andrae, U. Häußermann, M. Dolg, H. Stoll, H. Preuß, *Theor. Chim. Acta* **1990**, *77*, 123–141.

(18)   K. Fukui, *J. Phys. Chem.* **2005**, *74* (23), 4161–4163.

(19)   K. Fukui, *Acc. Chem. Res.* **1981**, *14*, 363–368.

(20)   A. V. Marenich, C. J. Cramer, D. G. Truhlar, *J. Phys. Chem. B* **2009**, *113*, 6378–6396.

(22)   S. Grimme, *Chem.: Eur. J.* **2012**, *18*, 9955–9964.

(22)   I. Funes-Ardoiz, R. S. Paton, GoodVibes v1.0.1 http://doi.org/10.5281/zenodo.56091.

(23)   L. Schrödinger, *The PyMOL Molecular Graphics Development Component, Version 1.8*; 2015.

(24)   S. E. Wheeler, K. N. Houk, P. V. R. Schleyer, W. D. Allen, *J. Am. Chem. Soc.* **2009**, *131*, 2547–2560.

(25)   S. E. Wheeler, **2012**, *2*, 204–220.

(26)   X. Zhang, G. Lu, M. Sun, M. Mahankali, Y. Ma, M. Zhang, W. Hua, Y. Hu, Q. Wang, J. Chen, *Nat. Chem.* **2018**, *10*, 540–548.

(27)   S. Porey, X. Zhang, S. Bhowmick, V. Kumar Singh, S. Guin; R. S. Paton, D. Maiti, *J. Am. Chem. Soc.* **2020**, *142*, 3762–3774.